Acta Cryst. (1999). A**55**, 1000–1013

X-ray intensity patterns from finite perfect crystals

Gunnar Thorkildsen* and Helge B. Larsen

Department of Mathematics and Natural Science, Stavanger College, Ullandhaug, N-4091 Stavanger, Norway.
E-mail: gunnar.thorkildsen@tn.his.no

(*Received 26 March 1999; accepted 4 June 1999*)

Abstract

A theoretical study dealing with intensity interference patterns from the exit surfaces of finite perfect $t \times l$ crystals has been undertaken using the Takagi–Taupin equations and the Riemann–Green technique. Numerical simulations have been performed for the 220 reflection in diamond allowing for different types of amplitude-modulated incoming plane waves. The effects caused by limiting the waves by a slit system are also discussed. The results show strong influence of the lateral crystal boundaries and are closely related to the geometrical region structures formed by the characteristic lines associated with the equations. In the limit of a semi-infinite crystal, the Borrmann–Lehmann interference patterns are retrieved.

1. Introduction

In a series of papers, we have investigated the influence of crystal boundaries on dynamical scattering in perfect crystals. So far questions related to extinction, ordinary absorption (Thorkildsen & Larsen, 1998*a*,*b*,*c*, 1999*a*; Larsen & Thorkildsen, 1998) and rocking curves (Thorkildsen & Larsen, 1999*c*) have been addressed. In the present work, we focus on the intensity patterns arising from the exit surfaces of finite perfect crystals subject to a monochromatic incident X-ray beam.

In 1963, Borrmann and Lehmann discovered a new type of interference contrast in section topographs where a point source was located in the vicinity of a crystal corner of a semi-infinite crystal plate (Borrmann & Lehmann, 1963; Lehmann & Borrmann, 1967). The resulting fringes were caused by multiple scattered waves owing to the vertical limiting crystal surface. The effect was re-investigated by Lang and co-workers (Lang *et al.*, 1986; Kowalski & Lang, 1986, 1987; Lang *et al.*, 1990) and Mai (Mai & Zhao, 1989) with the main objective to obtain accurate structure factors by analyzing the Borrmann–Lehmann fringe pattern.

In this analysis, we also discuss effects of nonsymmetrical reflection, various types of incoming waves that may have a limited extension owing to a slit system. Anomalous absorption is taken into account using a complex representation of the structure factors.

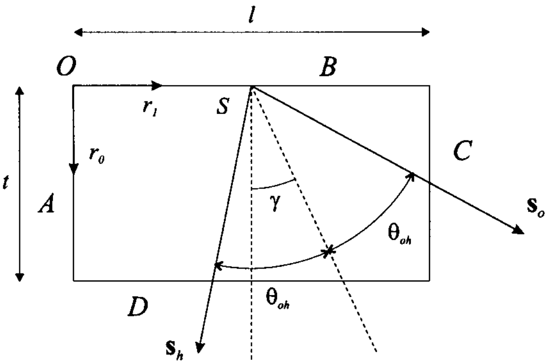

Fig. 1. Crystal dimensions, surface labels, coordinate systems and scattering geometry.

2. Theory

Various topics concerning X-ray scattering in *finite* perfect crystals are conveniently dealt with using the Takagi–Taupin equations (Takagi, 1962, 1969; Taupin, 1964). These include primary extinction, ordinary absorption, rocking curves and interference patterns (topography). The general theoretical foundation and the nomenclature applied have been thoroughly presented in previous papers (Thorkildsen & Larsen, 1998*a*,*b*,*c*, 1999*a*,*c*). We here only briefly outline the main points necessary to discuss features associated with the interference patterns arising from finite crystals. The crystal and scattering geometry, face labelling and actual coordinate systems are shown in Fig. 1.

The Takagi–Taupin equations for a perfect crystal are written in the representation†

$$\partial \tilde{D}_o / \partial s_o = i\kappa_{oh} \tilde{D}_h \qquad (1)$$

$$\partial \tilde{D}_h / \partial s_h = i\kappa_{ho} \tilde{D}_o. \qquad (2)$$

They may be transformed to:

$$\partial^2 \tilde{D}_p / \partial s_o \partial s_h + \kappa_{oh}\kappa_{ho} \tilde{D}_p = 0 \quad p \in (o, h). \qquad (3)$$

This is the canonical form of a second-order hyperbolic partial differential equation. Applying the Riemann–Green technique, the amplitude of the diffracted

---

† $\kappa_{pq} = -\pi K C \chi_{p-q} = (r_e \lambda C / V_c) F_{p-q}$; all symbols have their standard interpretation.

wavefield $\tilde{D}_h$ at a point P within the crystal is obtained from the integral equation

$$\tilde{D}_h(P) = (i\kappa_{ho}/\sin 2\theta_{oh}) \int_{S(P)} \mathbf{s}_o \cdot \mathrm{d}\mathbf{S}\, G_h(P|S)\tilde{D}_o^{(b)}(S). \qquad (4)$$

$i\kappa_{ho}G_h(P|S)$ is the boundary-value Green function or the *characteristic function*, the solution of the equation for the diffracted field subject to a point source at S, *i.e.* by applying the boundary condition $\tilde{D}_o^{(b)}(S) = \delta(s_h - s_h(S))$. The characteristic lines associated with equation (3) coincide with the coordinate axes. The boundaries of the crystal give rise to a multiple geometrical region structure separated by these lines (Uragami, 1969, 1970, 1971; Saka *et al.*, 1972*a*,*b*, 1973). To each region, m, a specific boundary-value Green function is assigned. The region structure and the corresponding family of Green functions depend on the position of the source point on the entrance surface of the crystal. For the $t \times l$ crystal considered, we have two different topologies† giving rise to a *Laue* and a *Bragg* situation, respectively, *cf.* Fig. 2. The actual region structures associated with Borrmann–Lehmann interference in semi-infinite crystals (Borrmann & Lehmann, 1963; Lehmann & Borrmann, 1967) are depicted in Fig. 3. It is evident that these cases occur as special limits of the general region structures.

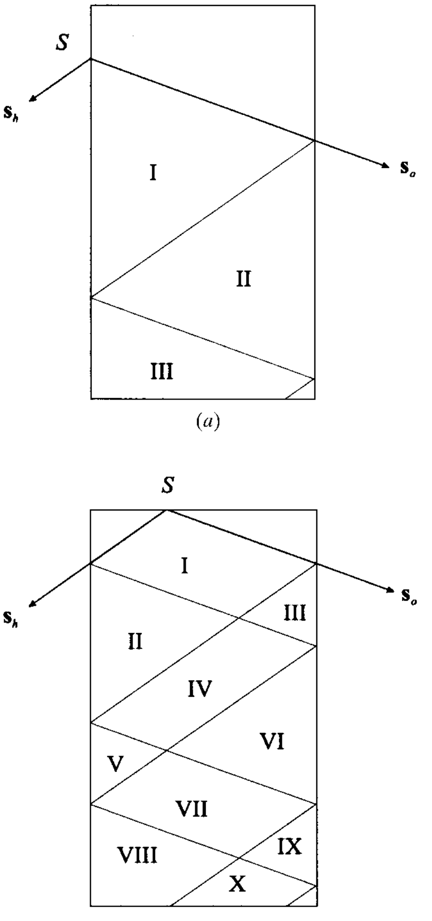

(*a*)

(*b*)

Fig. 2. (*a*) Bragg and (*b*) Laue families of regions.

We use a mathematical representation of the incoming and diffracted wave corresponding to amplitude modulated plane waves:

$$D_o(\mathbf{r}) = D_o^{(e)}(\mathbf{r}) \exp(-2\pi i\mathbf{K}_o\mathbf{r}) \qquad (5)$$

$$D_h(\mathbf{r}) = D_h^{(e)}(\mathbf{r}) \exp(-2\pi i\mathbf{K}_h\mathbf{r}). \qquad (6)$$

It has previously been shown (Thorkildsen & Larsen, 1998*a*) that the amplitude of the diffracted wave at the exit point M, expressed in the spatial variables (s_o, s_h), becomes:

$$\begin{aligned} D_h^{(e)}&[s_o(M), s_h(M)] \\ &= (i\kappa_{ho}/\sin 2\theta_{oh}) \int_{S(M)} \mathbf{s}_o \cdot \mathrm{d}\mathbf{S}\, D_o^{(e)}[s_o(S), s_h(S)] \\ &\quad \times G_h[u_0|s_o(M) - s_o(S), s_h(M) - s_h(S)] \\ &\quad \times \exp\{2\pi i\alpha_h[s_h(M) - s_h(S)]\} \exp\big(-\pi i K\chi_0 \\ &\quad \times \{[s_o(M) - s_o(S)] + [s_h(M) - s_h(S)]\}\big). \end{aligned} \qquad (7)$$

The range of integration covers that part of the entrance surface that gives rise to a diffracted field at M. The expansion parameter, $u_0 = \kappa_{oh}\kappa_{ho}$, is in general a complex quantity owing to resonance scattering effects.

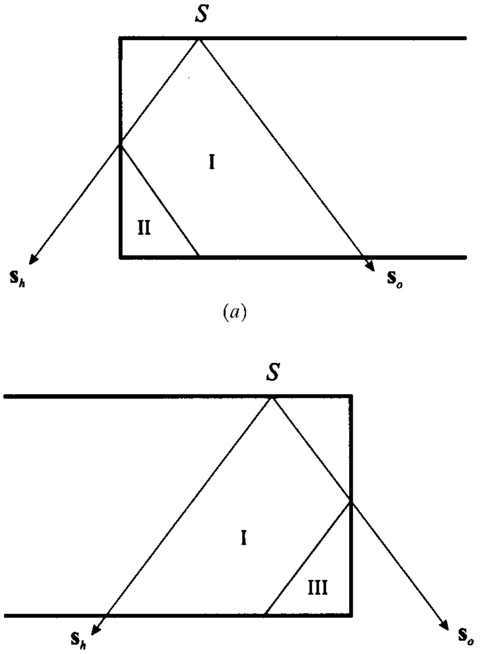

(*a*)

(*b*)

Fig. 3. Geometrical region structures in connection with Borrmann–Lehmann interference. (*a*) Type I (negative). (*b*) Type II (positive). Designation according to Lang *et al.* (1986).

---

† The asymmetry angle γ must satisfy equations (7) and (8) of Thorkildsen & Larsen (1999*a*).

Thus, anomalous absorption is incorporated by this representation (Kato, 1992). α_h is the excitation error, proportional to the deviation, $\Delta\theta_{oh}$, from the Bragg condition. χ_0, the average electric susceptibility, is also complex leading to refraction and ordinary absorption effects.

In what follows, we express the amplitude of the incoming wave by $D_o^{(e)}(\mathbf{r}) = D_o^{(e)} \times f(\mathbf{r})$. $f(\mathbf{r})$ represents the spatial modulation of the beam amplitude. Furthermore, the integration set-up in (7) is significantly simplified using a set of dimensionless coordinates† (x, y), respectively, related to the surface coordinates r_0 or r_1 of the source and exit point.

Once the amplitude of the displacement field is known at every point on the exit surfaces of the crystal, we may calculate:

(i) the intensity of the diffracted beam by the square modulus of the field amplitude;

(ii) the power of the diffracted beam by an integration of the intensity function across the exit surface(s);

(iii) the integrated power by an additional integration in the deviation parameter $\Delta\theta_{oh}$.

In this work, we focus on the intensity pattern. It is here formally expressed by

$$I_h(y|j) = I_o^{(e)}\, |\kappa_{ho}|^2 (tl/\sin 2\theta_{oh}) I_h^{(0)}(y|j) \qquad (8)$$

with

$$I_h^{(0)}(y|j) = (1/2\zeta) \Bigg| \sum_{i=A,B} \sum_{m=m'_{i-j}(y)} \int_{S_{i-j}(y,m)} \mathrm{d}x\, f(x) \times G_h^{i-j}(u|x,y|m) Q_h^{i-j}(x,y)\, A_h^{i-j}(x,y) \Bigg|^2 . \qquad (9)$$

In this equation, $j \in \{A, D\}$ denotes one of the exit surfaces. ζ is a geometrical parameter, $\zeta = (t/l)\tan\theta_{oh}$. The actual Green functions, $G_h^{i-j}(u|x,y|m)$ with $u = u_0\,(l/2\sin\theta_{oh})^2$, are given‡ in Thorkildsen & Larsen (1999*a*). The functions Q_h^{i-j} and A_h^{i-j} are related to refraction and ordinary absorption, *cf.* Thorkildsen & Larsen (1999*c*). They depend upon the dimensionless parameters $\xi_0 = (2l/\lambda)\cos\theta_{oh}$ and $\mu_0 = \mu\,(l/2\sin\theta_{oh})$, μ being the linear absorption coefficient.

The various modulating functions, $f(x)$, treated in this work are summarized below:

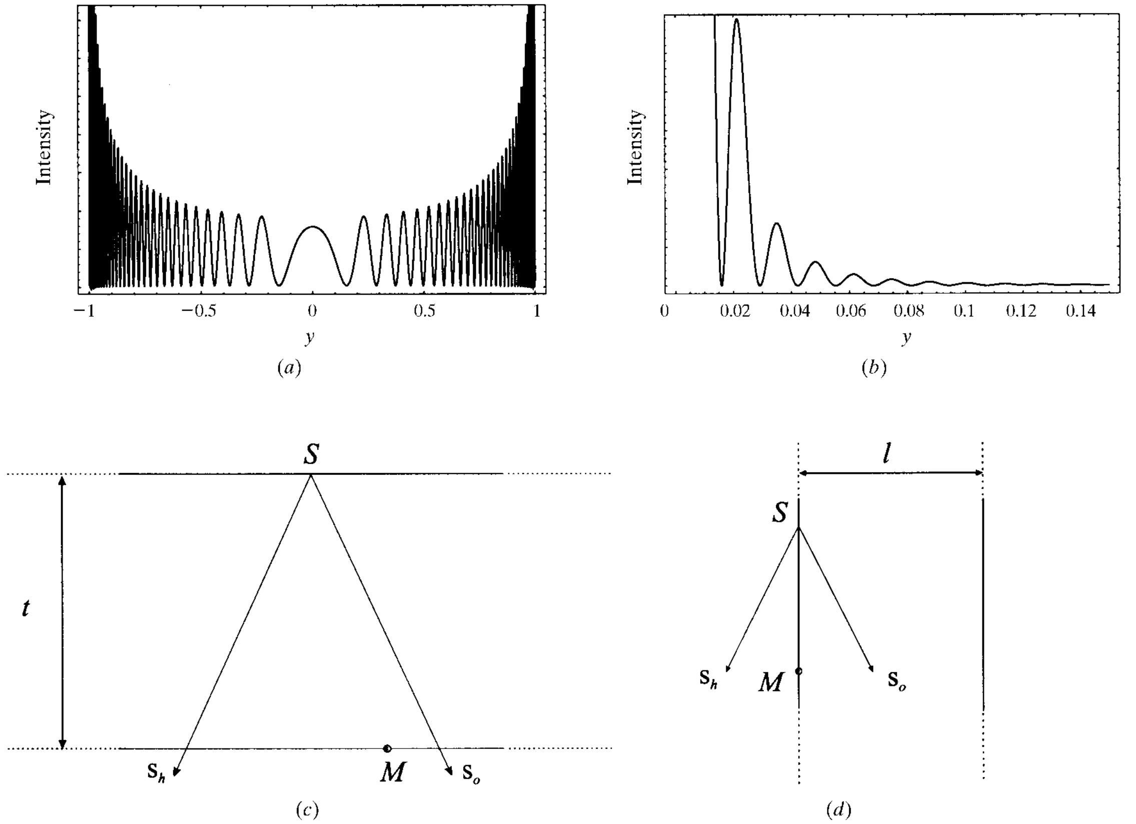

(*a*) (*b*)

(*c*) (*d*)

Fig. 4. Reference patterns for Laue and Bragg scattering, semi-infinite crystals, 220 reflection in diamond. Intensity in arbitrary units. The finite dimensions t or l are 1000 μm.

---

† Various representations are used for x and y depending on the actual problem.

‡ In the coordinate representation (s_o, s_h).

$$f(x) = \begin{cases} \delta(x - x_0) & \text{idealized point source} \\ 1 & \text{incident plane wave} \\ \exp[-\pi i \xi_s (x - x_0)^2] & \text{incident spherical wave.} \end{cases} \tag{10}$$

The parameter ξ_s is defined by

$$\xi_s = (l \cos\theta_{oh})^2/\lambda R, \tag{11}$$

R being the radius associated with the spherical wave. For this case, the derivation of $f(x)$ is given in Appendix *A*. The idealized point source may be viewed as the limit of the function

$$f(x) = \begin{cases} 1/\Delta & \text{when } x \in (x_0 - \Delta/2, x_0 + \Delta/2) \\ 0 & \text{otherwise} \end{cases}$$

when $\Delta \to 0$. In this case, the integration across the entrance surface of (9) is trivial owing to the appearance of the δ function. For the other two cases, the surface integration set-up is valign="top" more complex (Thorkildsen & Larsen, 1998*d*, 1999*b*). An interesting situation occurs if a slit is introduced to limit the spatial extension of the incoming beam. This is conveniently dealt with by redefining the actual range of the surface integration, *i.e.*

$$\int\limits_{S_{i-j}(y,m)} \mathrm{d}x \to \int\limits_{S_{i-j}(y,m)\cap(x_0-\Delta/2,x_0+\Delta/2)} \mathrm{d}x.$$

Δ is the width of the slit projected onto the actual entrance surface.

3. Results and discussion

3.1. *Scattering system*

The system used as basis for the simulations has been the 220 reflection in diamond. The value $a = 3.567$ Å was adopted for the lattice constant (Hom *et al.*, 1975). The structure factor was calculated at room temperature using atomic form factors from Waasmaier & Kirfel (1995), anomalous-scattering corrections based on the program *FPRIME* (Cromer & Liberman, 1970; Cromer, 1995) and the value $B = 0.143$ Å^2 for the Debye–Waller factor (Peng *et al.*, 1996). This gives the value $F_{220} = 15.39$, in agreement with the experimental value obtained by Takama *et al.* (1990). The extinction length Λ_{oh} becomes 10.5 µm,

$$\Lambda_{oh} \overset{\text{def}}{=} 1/(|\kappa_{oh}||\kappa_{ho}|)^{1/2}.$$

This corresponds to $\xi_g = 30.2$ µm, $\xi_g = \Lambda_{oh}(\pi \cos\theta_{oh})$ is the definition of the extinction length used by Lang *et al.* (1990). The wavelength of the incident X-ray beam was given the value 1.000 Å, and it was assumed to be in the σ-polarization state. Some other parameters are given in Table 1.

3.2. *Reference patterns*

Fig. 4 gives the standard intensity patterns for semi-infinite crystals. The intensity distribution associated with the Borrmann triangle for a point source on B (transmission case) is shown in Fig. 4(*a*). The geometrical region structure, Fig. 4(*c*), has only one region, $m = 1$, which is not affected by the lateral boundaries of the crystal. The intensity pattern for symmetrical scattering is modelled by (Authier, 1996)

Table 1. *Some parameters for diamond*

θ_{oh}: Bragg angle. $\Delta\theta^0_{oh}$: shift in Bragg angle. The dimensionless quantities ζ, u, ξ_0 and μ_0 refer to the crystal dimension $t \times l = 1000 \times 1000$ µm.

θ_{oh} (°)	$\Delta\theta^0_{oh}$ $(10^{-3})^\circ$	ζ	u	ξ_0	μ_0
23.358	0.747	0.432	$14500 + i33.3$	320.0	0.376

$$I_h(y) = |J_0\{2[\tilde{u}(1 - y^2)]^{1/2}\}|^2 \exp(-2\tilde{\mu}) \quad \text{with} \quad y \in (-1, 1), \tag{12}$$

where

$$\tilde{u} = \kappa_{oh}\kappa_{ho}(t/2\cos\theta_{oh})^2 \tag{13}$$

$$\tilde{\mu} = \mu t/2\cos\theta_{oh}. \tag{14}$$

$(t \tan\theta_{oh})y$ measures the lateral distance between the positions of the exit and source points. Fig. 4(*b*) shows the intensity distribution for a point source on A (reflection case), *cf.* Lang & Mai (1979). The characteristic line parallel to $\mathbf{s}_o$ does not encounter the 'back surface' of the crystal, *cf.* Fig. 4(*d*), thus we only need to take region $m = 1$, in principle of infinite extension, into account. (This corresponds to the Darwin case of Bragg scattering.) The intensity pattern, also for the case of symmetrical scattering, is modelled by (Uragami, 1971)

$$I_h(y) = |J_0(2u^{1/2}y) + J_2(2u^{1/2}y)|^2 \exp(-2\mu_0 y) \quad \text{with} \quad y \in (0, 2\cot\theta_{oh}). \tag{15}$$

ly measures the distance between exit and source point.

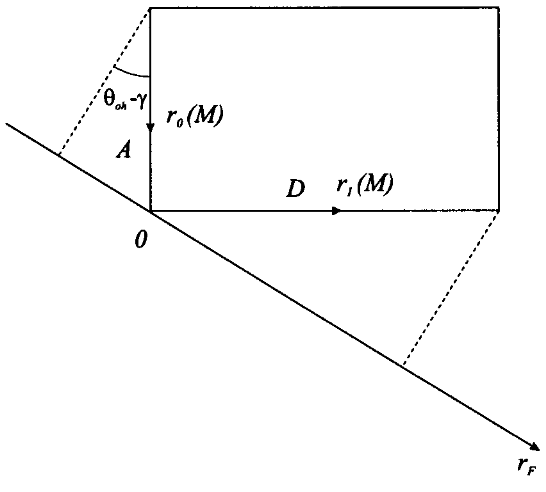

Fig. 5. Measuring the intensity along a common axis ⊥ $\mathbf{s}_h$.

3.3. *Recording the diffracted intensity*

In what follows, the intensity distribution from the exit surfaces A and D will be measured along a direction normal to $\mathbf{s}_h$, *cf.* Fig. 5. The actual coordinate is denoted by r_F. With the exit point M along the surface A, we have:†

$$r_F = -\sin\theta_{oh}(1/\beta_-)[t - r_o(M)],$$

while for M along D:

$$r_F = \cos\theta_{oh}(1/\delta_-)r_1(M)$$

Using the variable y here defined by the relations $r_0(M) = t\beta_- y/\zeta$ or $r_1(M) = l\delta_- y$ and introducing $z = r_F/t$, we obtain:

(i) When y measures the position along A:

$$z = -\sin\theta_{oh}(1/\beta_- - y/\zeta). \tag{16}$$

(ii) When y measures the position along D:

$$z = \sin\theta_{oh}(y/\zeta). \tag{17}$$

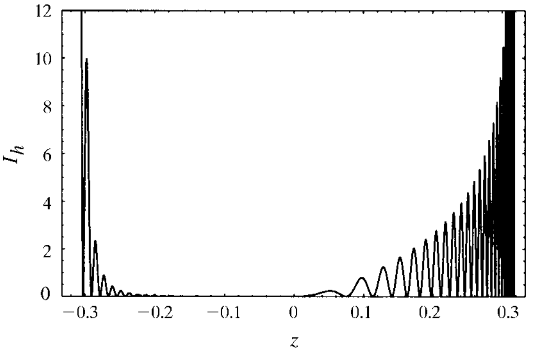

(*a*) $t \times l$ = 1000 × 500 μm

(*b*) $t \times l$ = 1000 × 200 μm

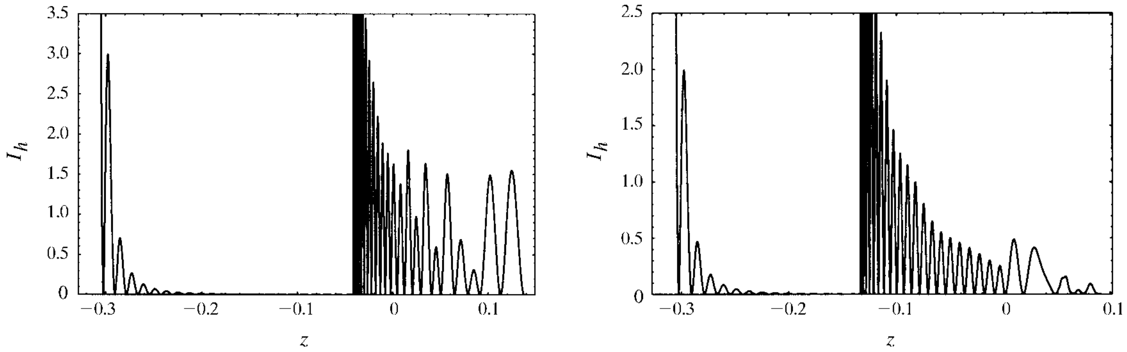

(*c*) $t \times l$ = 1000 × 150 μm

(*d*) $t \times l$ = 1000 × 100 μm

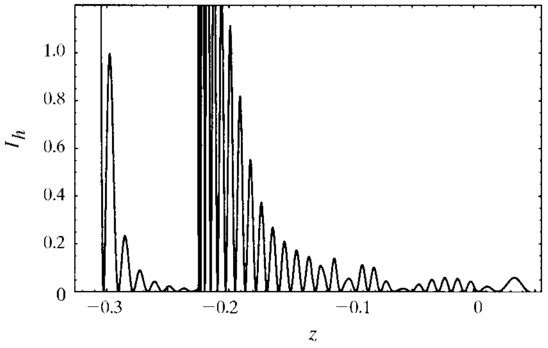

(*e*) $t \times l$ = 1000 × 50 μm

Fig. 6. Point-source intensity patterns – source on A. Intensity in units of 10^{-3}.

---

† The trigonometrical quantities $\beta_\pm$ and $\delta_\pm$ are given in Appendix B.

Table 2. *Contributions at the exit surfaces for a point source on A*

l	z	$i-j\,(m)$
500	(−0.317, 0.0)	$A-A\,(1)$
	(0.0, 0.317)	$A-D\,(1)$
200	(−0.317, 0.0)	$A-A\,(1)$
	(0.0, 0.050)	$A-D\,(1)$
	(0.050, 0.184)	$A-D\,(2)$
150	(−0.317, −0.0418)	$A-A\,(1)$
	(−0.0418, 0.0)	$A-A\,(3)$
	(0.0, 0.0418)	$A-D\,(3)$
	(0.0418, 0.138)	$A-D\,(2)$
100	(−0.317, −0.134)	$A-A\,(1)$
	(−0.134, 0.0)	$A-A\,(3)$
	(0.0, 0.0500)	$A-D\,(3)$
	(0.0500, 0.0918)	$A-D\,(4)$
50	(−0.317, −0.225)	$A-A\,(1)$
	(−0.225, −0.134)	$A-A\,(3)$
	(−0.134, −0.0418)	$A-A\,(5)$
	(−0.0418, 0.0)	$A-A\,(7)$
	(0.0, 0.0418)	$A-D\,(7)$
	(0.0418, 0.0459)	$A-D\,(6)$

Table 3. *Contributions at the exit surfaces for a point source on B*

l	z	$i-j\,(m)$
1000	(0.403, 0.641)	$B-D\,(1)$
	(0.641, 0.918)	$B-D\,(3)$
500	(−0.0564, 0.0)	$B-A\,(2)$
	(0.0, 0.0564)	$B-D\,(2)$
	(0.0564, 0.181)	$B-D\,(1)$
	(0.181, 0.459)	$B-D\,(3)$
400	(−0.148, 0.0)	$B-A\,(2)$
	(0.0, 0.0897)	$B-D\,(2)$
	(0.0897, 0.148)	$B-D\,(4)$
	(0.148, 0.367)	$B-D\,(3)$
300	(−0.240, −0.00212)	$B-A\,(2)$
	(−0.00212, 0.0)	$B-A\,(5)$
	(0.0, 0.00212)	$B-D\,(5)$
	(0.00212, 0.240)	$B-D\,(4)$
	(0.240, 0.275)	$B-D\,(3)$
200	(−0.332, −0.0939)	$B-A\,(2)$
	(−0.0939, 0.0)	$B-A\,(5)$
	(0.0, 0.0354)	$B-D\,(5)$
	(0.0354, 0.0939)	$B-D\,(7)$
	(0.0939, 0.184)	$B-D\,(6)$
150	(−0.378, −0.140)	$B-A\,(2)$
	(−0.140, −0.102)	$B-A\,(5)$
	(−0.102, 0.0)	$B-A\,(8)$
	(0.0, 0.102)	$B-D\,(8)$
	(0.102, 0.136)	$B-D\,(7)$
	(0.136, 0.138)	$B-D\,(9)$

3.4. *Intensity distributions owing to point sources*

In all the plots, I_h represents the quantity $I_h^{(0)}$ of equation (9) using z as the independent variable. In preparing the plots, we have not taken into account the effect of refraction at the exit boundaries. This causes angle deviations of the order of $\Re\chi_0 \approx 10^{-5}$. The deviations will also depend on the scattering situation $i-j$ and the asymmetry angle γ.

3.4.1. *Point source on A*. Fig. 6 shows the simulated intensity patterns with the point source located 200 µm from the upper left corner of the crystal. Fig. 7 depicts the associated geometrical region structures, while Table 2 gives the exact extension of the various scattering regions measured along z. The intensity scale has been chosen to amplify details, which means that the intensity enhancement close to the borders of region $m = 1$ is being cut. Fig. 6(*a*) comprises both a reflection case ($z < 0$) and a transmission case ($z > 0$). The influence

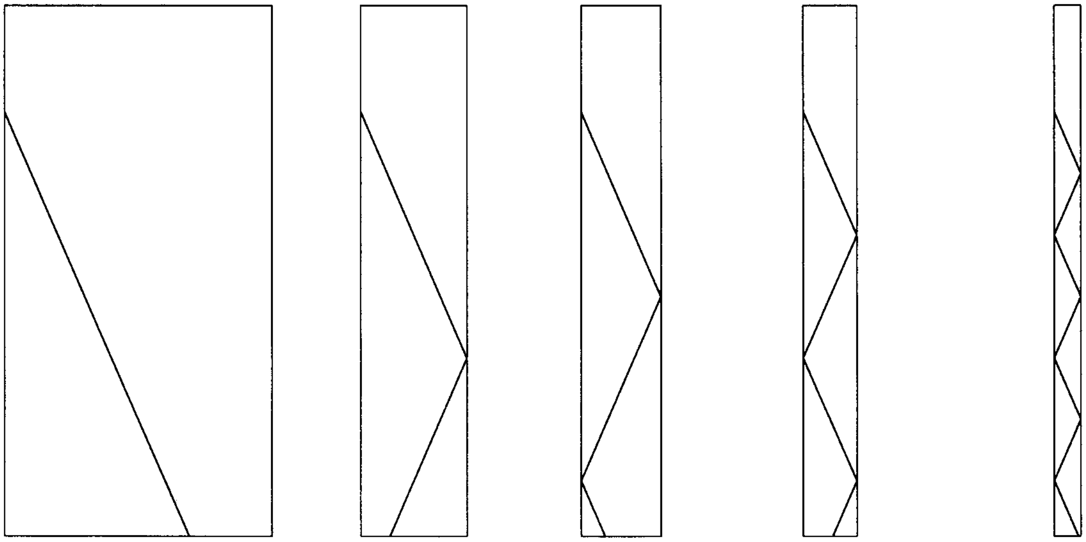
(*a*) (*b*) (*c*) (*d*) (*e*)

Fig. 7. Actual region structures – source on A. Position of source 200 µm from upper left corner. Crystal dimensions ($t \times l$): (*a*) 1000 × 500 µm, (*b*) 1000 × 200 µm, (*c*) 1000 × 150 µm, (*d*) 1000 × 100 µm, (*e*) 1000 × 50 µm.

of the 'back surface' is readily seen in Figs. 6(*b*)–6(*e*). It is evident that the $A - D$ contributions become less significant for increasing values of the ratio t/l. The fringe spacing for region $m = 3$, $A - A$ scattering, decreases when z is reduced towards the limiting value separating this region from that of $m = 1$. The mathematical structure of the associated Green function resembles the one for the pure Laue case, giving a denser fringe spacing close to the region border.

3.4.2. *Point source on B*. Fig. 8 shows the simulated intensity patterns with the point source located 130 µm to the left of the upper right corner of the crystal. Fig. 9 depicts the associated geometrical region structures, while Table 3 gives the intervals in z of the various scattering contributions. The situation addressed in Fig. 8(*a*) corresponds to the standard Borrmann–Lehmann pattern, type II, *cf.* Fig. 4 of Lang *et al.* (1990). The ratio t/ξ_g used in their work as a reference parameter has a value ~ 33.0 with the numerical input of Table 1. The Borrmann–Lehmann intensity distribution is associated with $B - D$ scattering, region $m = 3$. It is rather insensitive to changes of crystal dimension and may also be realized as a combined contribution from the regions $m = 3$ and $m = 4$, *e.g.* Figs. 8(*c*) and 8(*d*). Generally, the

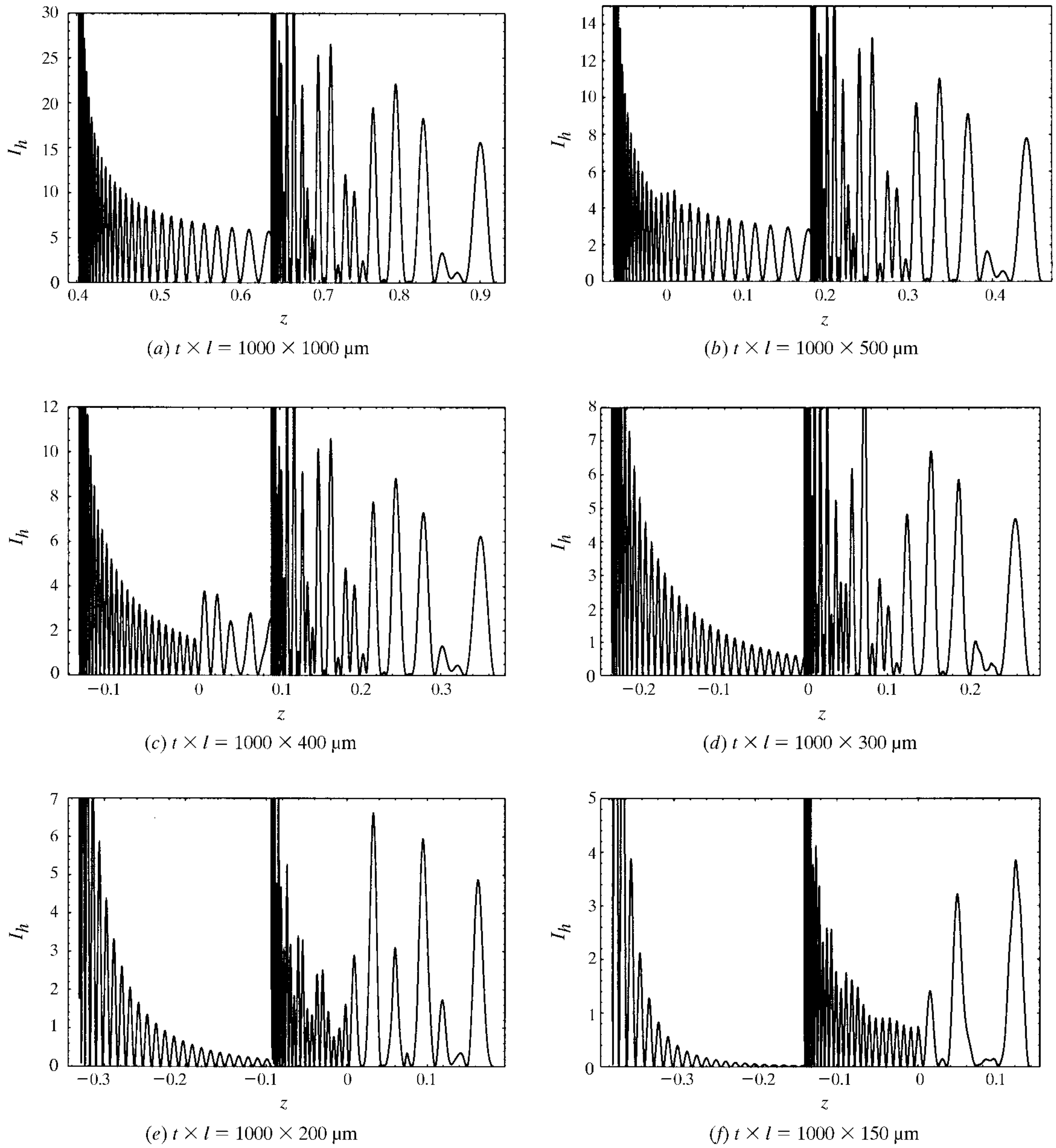

(*a*) $t \times l = 1000 \times 1000$ µm

(*b*) $t \times l = 1000 \times 500$ µm

(*c*) $t \times l = 1000 \times 400$ µm

(*d*) $t \times l = 1000 \times 300$ µm

(*e*) $t \times l = 1000 \times 200$ µm

(*f*) $t \times l = 1000 \times 150$ µm

Fig. 8. Point-source intensity patterns – source on B. Intensity in units of 10^{-3}.

fringe pattern has increased density close to the points defined by the projection on z of the characteristic lines parallel to $\mathbf{s}_h$ for $m = 1$. Contributions from higher-order $B - D$ regions show on the other hand a less dense fringe spacing. The fringe pattern is sensitive to nonsymmetrical scattering, as can be seen from Fig. 10, *cf.* also Fig. 11 and Table 4. Here the intensity distributions for a crystal with $t \times l = 1000 \times 300$ µm are shown for values of the asymmetry angle $\gamma = \pm 10°$. For the sake of completeness, the expressions giving the intensity distribution for the special Borrmann–Lehmann patterns in the case of nonsymmetrical scattering are included in Appendix B.

Table 4. *Contributions at the exit surfaces for a point source on B, nonsymmetrical scattering*

γ (°)	z	$i - j(m)$
−10	(−0.408, 0.0)	$B - A\,(2)$
	(0.0, 0.000726)	$B - D\,(2)$
	(0.000726, 0.147)	$B - D\,(4)$
	(0.147, 0.251)	$B - D\,(3)$
10	(−0.0652, 0.0)	$B - A\,(2)$
	(0.0, 0.106)	$B - D\,(2)$
	(0.106, 0.181)	$B - D\,(4)$
	(0.181, 0.292)	$B - D\,(3)$

3.5. *Intensity patterns owing to an incoming plane wave*

Fig. 12 depicts the intensity distributions for various crystal dimensions owing to an incoming plane wave. $\Delta\theta_{oh} = 0$ is applied for all simulations. Table 5 gives the scattering regions that contribute to the superposition of field amplitudes at different parts of the exit surfaces. The geometrical region structures depend upon ζ alone. This parameter is the same for the two cases illustrated in Figs. 12(a) and 12(b). The constant intensity level for $z \in (0.396, 0.522)$ is that of pure Laue transmission for the actual crystal thicknesses. Owing to the complexity of the intensity patterns, it is obvious that the calculation of the associated diffracted power will be difficult. For the intervals in z involving combined $A - A$ and $B - A$ scattering ($z < 0$) or $A - D$ and $B - D$ scattering ($z > 0$), the intensity patterns have both a super- and a sub- fringe structure. The superstructure depends on the geometrical parameter ζ. For the substructure, the fringe spacing seems to be approximately constant depending on the actual exit surface. Experimentally, a point-source situation may be realized using a slit to limit the

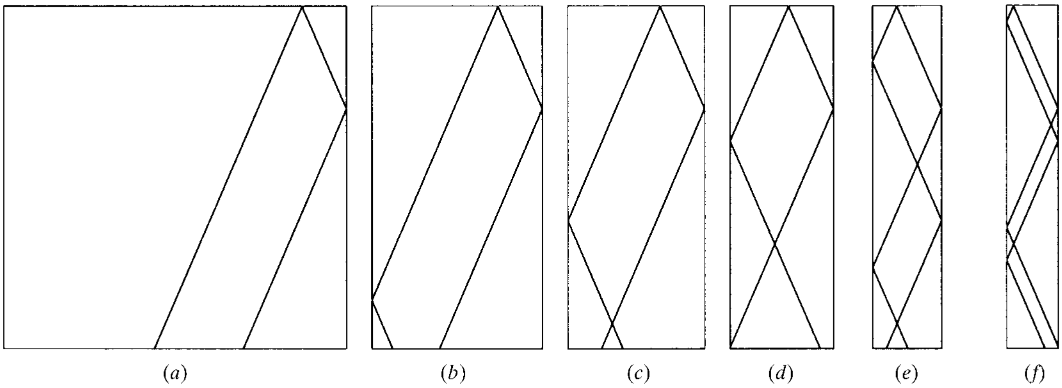
(*a*) (*b*) (*c*) (*d*) (*e*) (*f*)

Fig. 9. Actual region structures – source on B. Position of source 130 µm from upper right corner. Crystal dimensions ($t \times l$): (a) 1000 × 1000 µm, (b) 1000 × 500 µm, (c) 1000 × 400 µm, (d) 1000 × 300 µm, (e) 1000 × 200 µm, (f) 1000 × 150 µm.

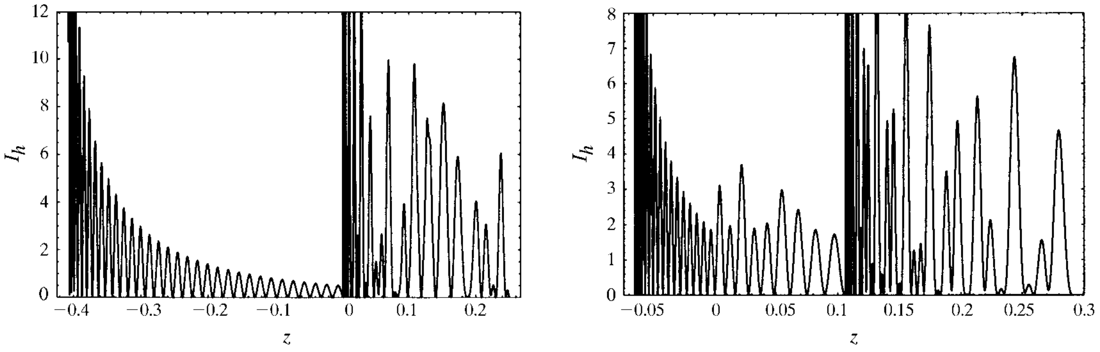

(a) $\gamma = -10°$ (b) $\gamma = 10°$

Fig. 10. Point-source intensity patterns for nonsymmetrical scattering – source on B. Intensity in units of 10^{-3}.

spatial extension of the incoming wave. Fig. 13 shows the effect of using a slit in connection with a plane wave. The slit gives an illuminated area of width Δ on the B surface centered at the position 130 μm from the upper right corner of the crystal. The crystal dimensions are 1000×1000 μm. With $\Delta = 1$ μm, there is complete agreement with the result based on the point-source formulation, *cf.* Fig. 8(*a*). By increasing the slit dimension, we observe that the part of the intensity distribution having fringe spacing less than Δ is averaged towards zero. This means that the Borrmann–Lehmann part of the intensity pattern remains unchanged for $\Delta \lesssim 20$ μm.

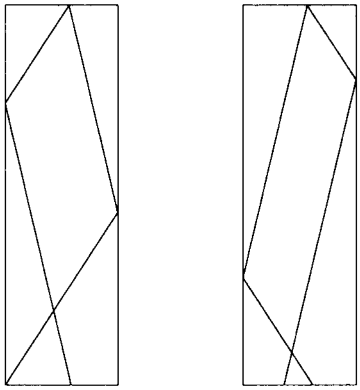
(*a*) $\gamma = -10°$ (*b*) $\gamma = 10°$

Fig. 11. Actual region structures for nonsymmetrical scattering – source on B. Position of source as in Fig. 9. Crystal dimensions: $t \times l = 1000 \times 300$ μm.

Table 5. *Contributions at the exit surfaces in the case of an incoming plane wave*

l	z	$i - j\,(m)$
1000	$(-0.396, 0.0)$	$A - A\,(1)$ $B - A\,(2)$
	$(0.0, 0.396)$	$A - D\,(1)$ $B - D\,(1, 2)$
	$(0.396, 0.522)$	$B - D\,(1)$
	$(0.522, 0.918)$	$B - D\,(1, 3)$
400	$(-0.396, -0.0293)$	$A - A\,(1)$ $B - A\,(2)$
	$(-0.0293, 0.0)$	$A - A\,(1)$ $B - A\,(2, 5)$
	$(0.0, 0.0293)$	$A - D\,(1)$ $B - D\,(2, 4, 5)$
	$(0.0293, 0.338)$	$A - D\,(1)$ $B - D\,(2, 3, 4)$
	$(0.338, 0.367)$	$A - D\,(1, 2)$ $B - D\,(3, 4, 6)$
200	$(-0.396, -0.213)$	$A - A\,(1)$ $B - A\,(2)$
	$(-0.213, -0.0293)$	$A - A\,(1)$ $B - A\,(2, 5)$
	$(-0.0293, 0.0)$	$A - A\,(1)$ $B - A\,(5, 8)$
	$(0.0, 0.0293)$	$A - D\,(1, 2, 3)$ $B - D\,(5, 7, 8)$
	$(0.0293, 0.154)$	$A - D\,(1, 2)$ $B - D\,(5, 6, 7)$
	$(0.154, 0.184)$	$A - D\,(1, 2)$ $B - D\,(6, 7, 9)$

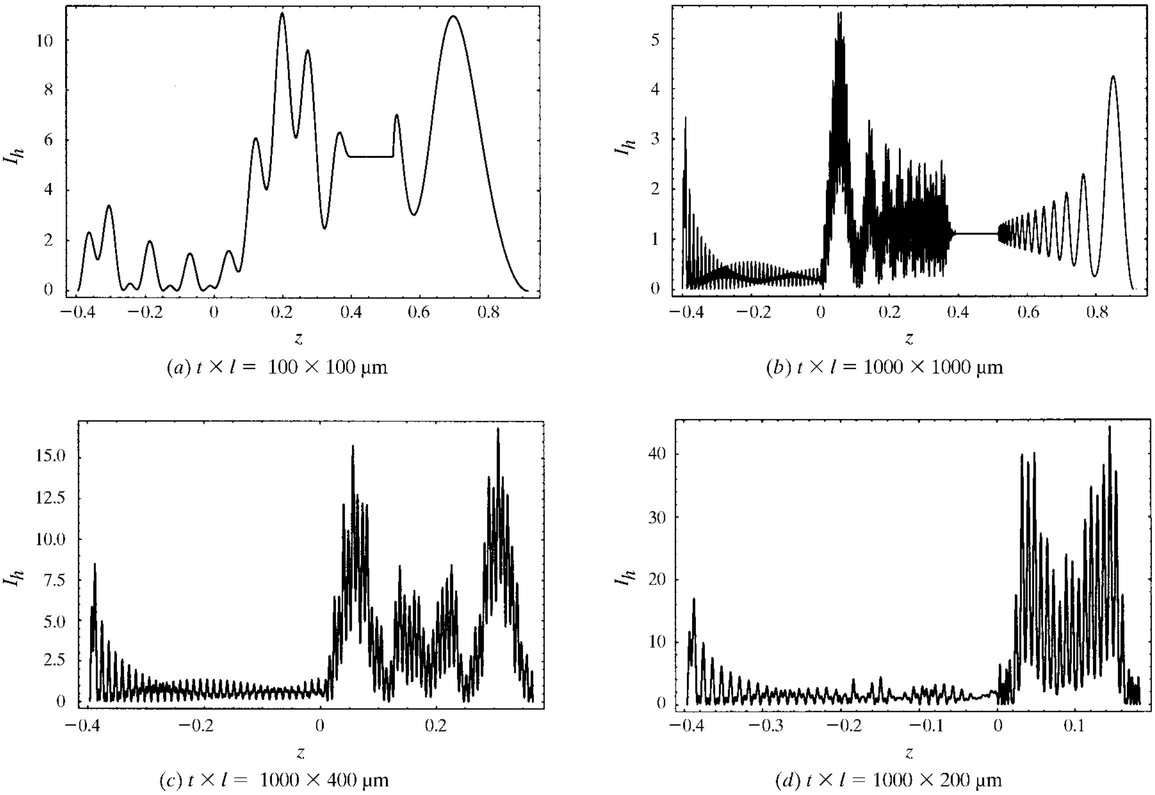

(*a*) $t \times l = 100 \times 100$ μm (*b*) $t \times l = 1000 \times 1000$ μm

(*c*) $t \times l = 1000 \times 400$ μm (*d*) $t \times l = 1000 \times 200$ μm

Fig. 12. Intensity patterns owing to an incoming plane wave. Intensity in units of 10^{-3} (*a*) or 10^{-5} (*b*)–(*d*).

3.6. *Spherical waves*

In the context of standard dynamical theory, the concept of a point source is related to an incoming spherical wave (Kato, 1961*a*,*b*, 1968*a*,*b*; Azároff *et al.*, 1974). By using the stationary-phase method (Jones, 1966; Jeffreys & Jeffreys, 1972), we have in the limit $\xi_s \rightarrow \infty$:

$$\int \mathrm{d}x \, \exp[-\pi i \xi_s (x - x_0)^2] G_h^{i-j}(x, y) \approx (1/\xi_s)^{1/2} \exp(-i\pi/4) G_h^{i-j}(x_0, y). \qquad (18)$$

Thus, the intensity pattern arising from a crystal subject to an incoming spherical wave is given by the one calculated from the concept of a mathematical point source. The application of the stationary-phase method requires however that the parameter ξ_s, given by (11), becomes large. This requirement may not be fulfilled for finite crystals. Fig. 14 shows the intensity pattern arising from a 50 × 50 μm crystal subject to incoming spherical waves having different radii R. x_0 is zero, thus the reference direction is from the beam source to the upper left corner of the crystal, point O, *cf.* Fig. 1. $\Delta\theta_{oh}$ associated with this direction is set to zero in the simulations. For $R = 100$ m, the intensity pattern is identical to that of an incoming plane wave. For decreasing values of R, the intensity patterns change significantly. Fig. 15 gives the expected final result from the point-source approach. It is clear that this limit is not reached even for $R = 0.1$ m. It should be mentioned that for increasing values of ξ_s the integrand oscillates so rapidly that it is difficult to obtain proper convergence in the numerical integrations.† This problem first arises for those exit points involving the largest path lengths measured from O.

Fig. 16 shows simulations that incorporate the effect of a slit in connection with an incoming spherical wave of radius $R = 1$ m. The crystal size is 1000 × 1000 μm. The reference point x_0 has the same position as that used for the simulations with a point source on the B surface. For the smallest slit size, the result is the same as for a point source. Increasing the slit size seems to have little effect on the typical Borrmann–Lehmann features of the pattern, contrary to what was found for the case of a plane wave.

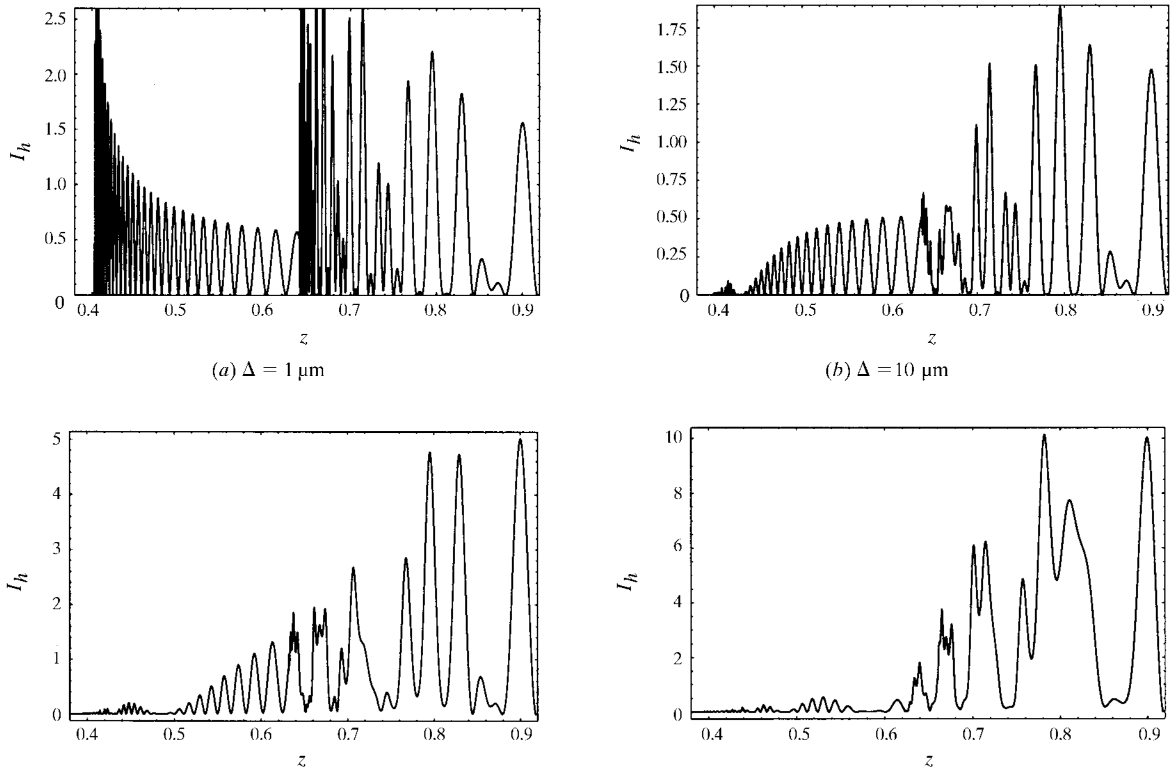

(*a*) Δ = 1 μm (*b*) Δ = 10 μm

(*c*) Δ = 20 μm (*d*) Δ = 40 μm

Fig. 13. Intensity patterns owing to an incoming plane wave limited by a slit giving an illuminated area of width Δ. Intensity in units of 10^{-8} (*a*) or 10^{-6} (*b*)–(*d*).

---

† The numerical calculations are performed using the mathematical software system *Mathematica* (Wolfram, 1996).

4. Conclusions

The use of the Takagi–Taupin equations along with the Riemann–Green technique has proved to be a powerful tool in the analysis of dynamical diffraction features from finite perfect crystals. In the particular context of intensity calculation, equation (9) represents the key result. The introduction of the modulating function, $f(x)$, also adds the possibility of studying various types of waves impinging the crystal within the same mathematical framework. In the limit of a semi-infinite crystal, the Borrmann–Lehmann results are obtained. New extended expressions including nonsymmetrical scattering are given for these cases.

The series of simulations presented for the 220 reflection in finite $t \times l$ perfect diamond crystals shows that the influence of the lateral crystal surfaces strongly affects the resulting intensity patterns. Furthermore, even small changes in the input parameters may cause significant alterations in the picture. From an experimental point of view, this is important. It is crucial to design an experiment in such a way that all parameters (crystal geometry, reflection asymmetry, slit size, position of point source *etc.*) are known to great accuracy. The interference patterns produced by the crystal itself are complex and may have a detailed fringe structure. This may be difficult to resolve experimentally. However, the potential of using such patterns for accu-

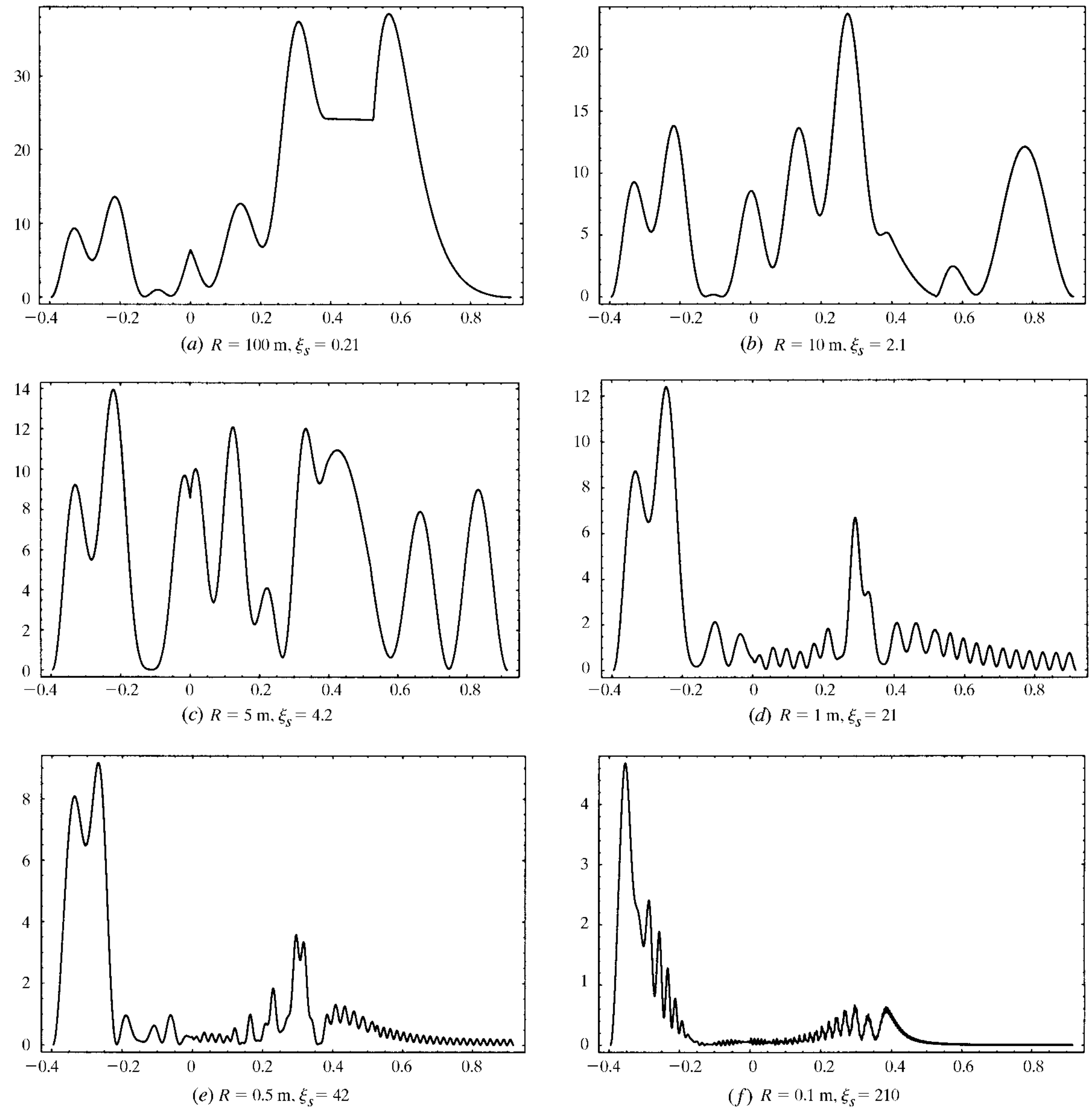

(*a*) $R = 100$ m, $\xi_s = 0.21$

(*b*) $R = 10$ m, $\xi_s = 2.1$

(*c*) $R = 5$ m, $\xi_s = 4.2$

(*d*) $R = 1$ m, $\xi_s = 21$

(*e*) $R = 0.5$ m, $\xi_s = 42$

(*f*) $R = 0.1$ m, $\xi_s = 210$

Fig. 14. Intensity patterns owing to an incoming spherical wave. Ordinate: intensity in units of 10^{-3}. Abscissa: 'film' coordinate z.

rate determination of the structure factor, as suggested by Lang *et al.*, is still evident. It may however be a severe experimental challenge to specify/control all parameters needed for a proper theoretical interpretation.

APPENDIX *A*
A spherical wave represented by an amplitude-modulated plane wave

Fig. 17 shows some geometrical quantities used in this section. This derivation closely follows the work of Authier & Simon (1968). The expression for a spherical wave,

$$\Phi_o \exp(-2\pi i K r)/4\pi r,$$

is expanded as

$$D_o(\mathbf{r}) = (\Phi_o/4\pi r)\exp[-2\pi i(Kr - \mathbf{K}_o\cdot\mathbf{r})] \times \exp(-2\pi i\mathbf{K}_o\cdot\mathbf{r}). \qquad (19)$$

The reference wavevector $\mathbf{K}_o = \mathbf{s}_o/\lambda$ and the direction $\mathbf{r}(S_0)$ is parallel to $\mathbf{s}_o$. $\Delta\theta_{oh}$ is calculated with respect to $\mathbf{K}_o$. At the boundary, we have

$$\mathbf{r} = \mathbf{r}(S) = \mathbf{r}(S_0) + \mathbf{d}(S) \quad \text{and} \quad |\mathbf{r}(S_0)| \overset{\text{def}}{=} R.$$

To second order in $d = |\mathbf{d}(S)|$, the amplitude at the entrance point (S) is given by

$$D_o^{(e)}(S) = (\Phi_o/4\pi R)\exp\left(-\pi i(1/\lambda R)\{d^2 - [\hat{s}_o\cdot\mathbf{d}(S)]^2\}\right). \qquad (20)$$

In the general case of nonsymmetrical scattering, this expression becomes:

(i) Source on *A*:

$$D_o^{(e)}(S) = (\Phi_o/4\pi R)\exp\{-\pi i(1/\lambda R)\sin^2\theta_{oh}(1/\beta_+^2) \times [r_0(S) - r_0(S_0)]^2\}.$$

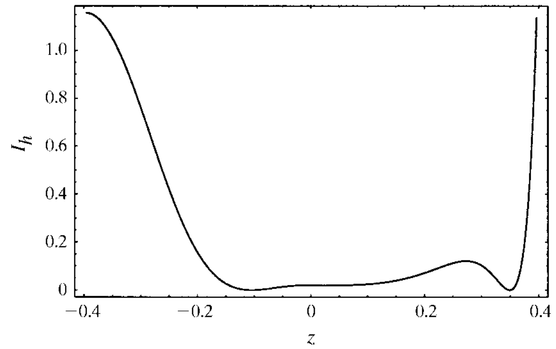

Fig. 15. Intensity pattern owing to a point source at *O*.

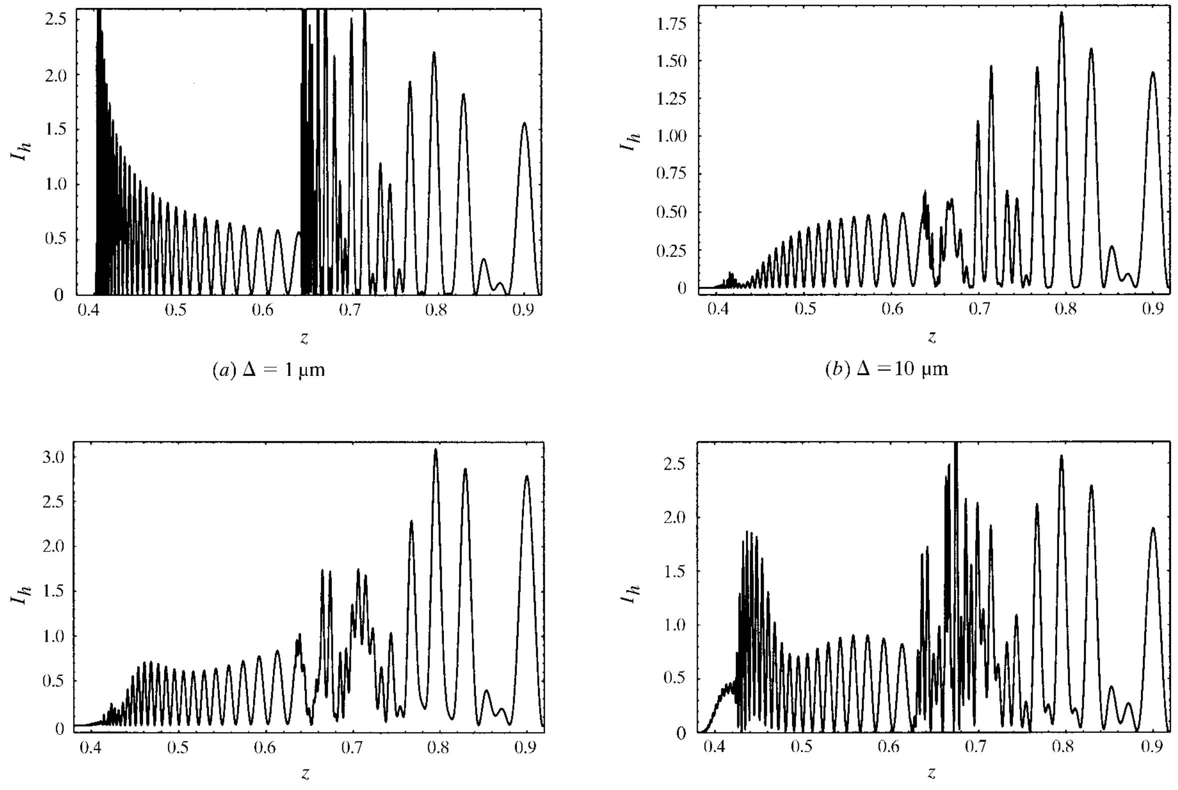

(*a*) $\Delta = 1$ μm

(*b*) $\Delta = 10$ μm

(*c*) $\Delta = 20$ μm

(*d*) $\Delta = 40$ μm

Fig. 16. Intensity patterns owing to an incoming spherical wave limited by a slit. Intensity in units of 10^{-8} (*a*) or 10^{-6} (*b*)–(*d*). $\xi_s = 8.4 \times 10^3$.

(ii) Source on B:

$$\begin{aligned} D_o^{(e)}(S) &= (\Phi_o/4\pi R)\exp\{-\pi i(1/\lambda R)\cos^2\theta_{oh}(1/\delta_+^2) \\ &\quad\times[r_1(S)-r_1(S_0)]^2\}. \end{aligned}$$

With the introduction of dimensionless variables, we have:

(i) For $A-A$ and $A-D$ scattering:

$$r_0(S)-r_0(S_0)=\cot\theta_{oh}\beta_+ l(x_0-x).$$

(ii) For $B-A$ and $B-D$ scattering:

$$r_1(S)-r_1(S_0)=\delta_+ l(x-x_0).$$

It turns out that the field at any entrance point may be expressed by the relation

$$D_o^{(e)}(x)=(\Phi_o/4\pi R)\exp[-\pi i\xi_s(x-x_0)^2]. \tag{21}$$

APPENDIX *B*
General expressions for Borrmann–Lehmann intensity patterns

We here present the general expressions, with allowance for nonsymmetrical scattering, for the Borrmann–Lehmann intensity patterns, *cf.* Fig. 3. The following definitions apply:

$$\beta_\pm=\sin\theta_{oh}/\sin(\theta_{oh}\pm\gamma) \tag{22}$$

$$\delta_\pm=\cos\theta_{oh}/\cos(\theta_{oh}\pm\gamma). \tag{23}$$

*B*1. *Type I pattern*

The variable x is defined by $r_1(S)=tx$, while y is defined by $r_0(M)=t+ty$ or $r_1(M)=ty$ for exit points on surface A or D, respectively. The type I interference pattern is realized when $x\in(0,\tan\theta_{oh}[\delta_-/\beta_-])$:

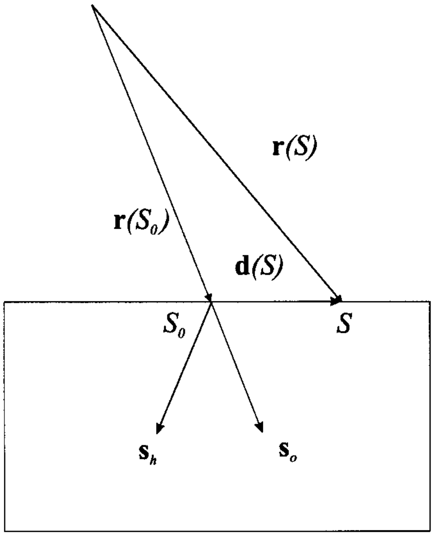

Fig. 17. Geometry used for derivation of the amplitude modulating function in the case of a spherical wave.

*B*1.1. *B–A scattering – region II.* For $y\in(\cot\theta_{oh}[\beta_-/\delta_-]x-1,0)$:

$$\begin{aligned} I_h(x,y) &= \Bigl|J_0\bigl(2\{\tilde{u}(1/\beta_+\beta_-)[(1+y)+\cot\theta_{oh}(\beta_+/\delta_+)x] \\ &\quad\times[(1+y)-\cot\theta_{oh}(\beta_-/\delta_-)x]\}^{1/2}\bigr) \\ &\quad+\frac{(1+y)-\cot\theta_{oh}(\beta_-/\delta_-)x}{(1+y)+\cot\theta_{oh}(\beta_+/\delta_+)x} \\ &\quad\times J_2\bigl(2\{\tilde{u}(1/\beta_+\beta_-)[(1+y)+\cot\theta_{oh}(\beta_+/\delta_+)x] \\ &\quad\times[(1+y)-\cot\theta_{oh}(\beta_-/\delta_-)x]\}^{1/2}\bigr)\Bigr|^2 \\ &\quad\times\exp\{-\tilde{\mu}[(1/\beta_++1/\beta_-)(1+y) \\ &\quad+\cot\theta_{oh}(1/\delta_+-1/\delta_-)x]\}. \end{aligned} \tag{24}$$

*B*1.2. *B–D scattering – region II.* For $y\in(0,[\delta_+/\beta_+]\{\tan\theta_{oh}-[\beta_-/\delta_-]x\})$:

$$\begin{aligned} I_h(x,y) &= \Bigl|J_0\bigl(2\{\tilde{u}(1/\beta_+\beta_-)[1+\cot\theta_{oh}(\beta_-/\delta_-)(y-x)] \\ &\quad\times[1-\cot\theta_{oh}(\beta_+/\delta_+)(y-x)]\}^{1/2}\bigr) \\ &\quad+\frac{1-\cot\theta_{oh}[(\beta_+/\delta_+)y+(\beta_-/\delta_-)x]}{1+\cot\theta_{oh}[(\beta_-/\delta_-)y+(\beta_+/\delta_+)x]} \\ &\quad\times J_2\Bigl[2\bigl(\tilde{u}(1/\beta_+\beta_-)\{1+\cot\theta_{oh}[(\beta_-/\delta_-)y \\ &\quad+(\beta_+/\delta_+)x]\}\{1-\cot\theta_{oh}[(\beta_+/\delta_+)y \\ &\quad+(\beta_-/\delta_-)x]\}\bigr)^{1/2}\Bigr]\Bigr|^2\exp\{-\tilde{\mu}[(1/\beta_++1/\beta_-) \\ &\quad-\cot\theta_{oh}(1/\delta_+-1/\delta_-)(y-x)]\}. \end{aligned} \tag{25}$$

*B*1.3. *B–D scattering – region I.* For $y\in([\delta_+/\beta_+]\{\tan\theta_{oh}-[\beta_-/\delta_-]x\},\tan\theta_{oh}[\delta_+/\beta_+]+x)$:

$$\begin{aligned} I_h(x,y) &= \Bigl|J_0\bigl(2\{\tilde{u}(1/\beta_+\beta_-)[1+\cot\theta_{oh}(\beta_-/\delta_-)(y-x)] \\ &\quad\times[1-\cot\theta_{oh}(\beta_+/\delta_+)(y-x)]\}^{1/2}\bigr)\Bigr|^2 \\ &\quad\times\exp\{-\tilde{\mu}[(1/\beta_++1/\beta_-) \\ &\quad-\cot\theta_{oh}(1/\delta_+-1/\delta_-)(y-x)]\}. \end{aligned} \tag{26}$$

*B*2. *Type II pattern*

The variable x is now defined by $r_1(S)=l-tx$, while y is defined by $r_1(M)=l-ty$. The type II interference pattern is realized when $x\in(0,\tan\theta_{oh}[\delta_+/\beta_+])$:

*B*2.1. *B–D scattering – region III.* For $y\in(0,[\delta_-/\beta_-]\{\tan\theta_{oh}-[\beta_+/\delta_+]x\})$:

$$\begin{aligned} I_h(x,y) = {} & \big|J_0\big(2\{\tilde{u}(1/\beta_+\beta_-)[1+\cot\theta_{oh}(\beta_-/\delta_-)(x-y)] \\ & \times[1-\cot\theta_{oh}(\beta_+/\delta_+)(x-y)]\}^{1/2}\big) \\ & - J_0\big[2\big(\tilde{u}(1/\beta_+\beta_-)\{1+\cot\theta_{oh}[(\beta_-/\delta_-)x \\ & + (\beta_+/\delta_+)y]\}\{1-\cot\theta_{oh}[(\beta_+/\delta_+)x \\ & + (\beta_-/\delta_-)y]\}\big)^{1/2}\big]\big|^2 \exp\{-\tilde{\mu}[(1/\beta_+ + 1/\beta_-) \\ & - \cot\theta_{oh}(1/\delta_+ - 1/\delta_-)(x-y)]\}. \end{aligned} \tag{27}$$

B2.2. B–D scattering – region I. For $y \in ([\delta_-/\beta_-]\{\tan\theta_{oh} - [\beta_+/\delta_+]x\}, \tan\theta_{oh}[\delta_-/\beta_-] + x)$:

$$\begin{aligned} I_h(x,y) = {} & \big|J_0\big(2\{\tilde{u}(1/\beta_+\beta_-)[1+\cot\theta_{oh}(\beta_-/\delta_-)(x-y)] \\ & \times[1-\cot\theta_{oh}(\beta_+/\delta_+)(x-y)]\}^{1/2}\big)\big|^2 \\ & \times \exp\{-\tilde{\mu}[(1/\beta_+ + 1/\beta_-) \\ & - \cot\theta_{oh}(1/\delta_+ - 1/\delta_-)(x-y)]\}. \end{aligned} \tag{28}$$

References

Authier, A. (1996). *Proceedings, X-ray and Neutron Dynamical Diffraction. Theory and Applications*, *NATO ASI Series, Series B: Physics*, Vol. 357, edited by A. Authier, S. Lagomarsino & B. Tanner, pp. 1–31. New York: Plenum.

Authier, A. & Simon, D. (1968). *Acta Cryst.* A**24**, 517–526.

Azároff, L. V., Kaplow, R., Kato, N., Weiss, R., Wilson, A. J. C. & Young, R. A. (1974). *X-ray Diffraction.* New York: McGraw-Hill.

Borrmann, G. & Lehmann, K. (1963). *Crystallography and Crystal Perfection*, Vol. A, edited by G. N. Ramachandran, pp. 101–108. New York: Academic Press.

Cromer, D. (1995). Private communication.

Cromer, D. & Liberman, D. (1970). *J. Chem. Phys.* **53**, 1891–1898.

Hom, T., Kiszenik, W. & Post, B. (1975). *J. Appl. Cryst.* **8**, 457.

Jeffreys, H. & Jeffreys, B. (1972). *Methods of Mathematical Physics.* Cambridge University Press.

Jones, D. S. (1966). *Generalized Functions.* London: McGraw-Hill.

Kato, N. (1961*a*). *Acta Cryst.* **14**, 526–532.

Kato, N. (1961*b*). *Acta Cryst.* **14**, 627–636.

Kato, N. (1968*a*). *J. Appl. Phys.* **39**, 2225–2230.

Kato, N. (1968*b*). *J. Appl. Phys.* **39**, 2231–2237.

Kato, N. (1992). *Acta Cryst.* A**48**, 829–834.

Kowalski, G. & Lang, A. R. (1986). *J. Appl. Cryst.* **19**, 224–228.

Kowalski, G. & Lang, A. R. (1987). *Acta Cryst.* A**43**, C220.

Lang, A. R., Kowalski, G. & Makepeace, P. W. (1990). *Acta Cryst.* A**46**, 215–227.

Lang, A. R., Kowalski, G., Makepeace, P. W. & Moore, M. (1986). *Acta Cryst.* A**42**, 501–510.

Lang, A. R. & Mai, Z.-H. (1979). *Proc. R. Soc. London Ser. A*, **368**, 313–329.

Larsen, H. B. & Thorkildsen, G. (1998). *Acta Cryst.* A**54**, 511–512.

Lehmann, K. & Borrmann, G. (1967). *Z. Kristallogr.* **125**, 234–248.

Mai, Z.-H. & Zhao, H. (1989). *Acta Cryst.* A**45**, 602–609.

Peng, L.-M., Ren, G., Dudarev, S. & Whelan, M. (1996). *Acta Cryst.* A**52**, 456–470.

Saka, T., Katagawa, T. & Kato, N. (1972*a*). *Acta Cryst.* A**28**, 102–113.

Saka, T., Katagawa, T. & Kato, N. (1972*b*). *Acta Cryst.* A**28**, 113–120.

Saka, T., Katagawa, T. & Kato, N. (1973). *Acta Cryst.* A**29**, 192–200.

Takagi, S. (1962). *Acta Cryst.* **15**, 1311–1312.

Takagi, S. (1969). *J. Phys. Soc. Jpn*, **26**, 1239–1253.

Takama, T., Tsuchiya, K., Kobayashi, K. & Sato, S. (1990). *Acta Cryst.* A**46**, 514–517.

Taupin, D. (1964). *Bull. Soc. Fr. Minéral. Cristallogr.* **87**, 469–511.

Thorkildsen, G. & Larsen, H. B. (1998*a*). *Acta Cryst.* A**54**, 172–185.

Thorkildsen, G. & Larsen, H. B. (1998*b*). *Acta Cryst.* A**54**, 186–190.

Thorkildsen, G. & Larsen, H. B. (1998*c*). *Acta Cryst.* A**54**, 416–429.

Thorkildsen, G. & Larsen, H. B. (1998*d*). *Two Beam Diffraction in Perfect Crystals Analyzed by Takagi's Equations. Part 3. Rocking Curves & Intensity Distributions.* Technical Report 42, Stavanger College, Stavanger, Norway.

Thorkildsen, G. & Larsen, H. B. (1999*a*). *Acta Cryst.* A**55**, 1–13.

Thorkildsen, G. & Larsen, H. B. (1999*b*). *Two Beam Diffraction in Perfect Crystals Analyzed by Takagi's Equations. Part 5. Mathematica-setup for Intensity Distribution Calculations*. Technical Report, Stavanger College, Stavanger, Norway. In preparation.

Thorkildsen, G. & Larsen, H. B. (1999*c*). *Acta Cryst.* A**55**, 840–854.

Uragami, T. S. (1969). *J. Phys. Soc. Jpn*, **27**, 147–154.

Uragami, T. S. (1970). *J. Phys. Soc. Jpn*, **28**, 1508–1527.

Uragami, T. S. (1971). *J. Phys. Soc. Jpn*, **31**, 1141–1161.

Waasmaier, D. & Kirfel, A. (1995). *Acta Cryst.* A**51**, 416–431.

Wolfram, S. (1996). *The Mathematica Book*, 3rd ed. Champain, IL 61820, USA: Wolfram Media/Cambridge University Press.